Characterization of the pressure-induced phase transition of metallization for MoTe$_2$ under hydrostatic and non-hydrostatic conditions

Linfei Yang, Lidong Dai (iD), Heping Li (iD), Haiying Hu, Kaixiang Liu, Chang Pu, Meiling Hong, and Pengfei Liu

View Online   Export Citation   CrossMark

Characterization of the pressure-induced phase transition of metallization for MoTe₂ under hydrostatic and non-hydrostatic conditions

View Online   Export Citation   CrossMark

Linfei Yang,[1,2] Lidong Dai,[1,a] (iD) Heping Li,[1] (iD) Haiying Hu,[1] Kaixiang Liu,[1,2] Chang Pu,[1,2] Meiling Hong,[1,2] and Pengfei Liu[3]

AFFILIATIONS

[1] Key Laboratory of High-Temperature and High-Pressure Study of the Earth's Interior, Institute of Geochemistry, Chinese Academy of Sciences, Guiyang, Guizhou 550081, China
[2] University of Chinese Academy of Sciences, Beijing 100049, China
[3] State Key Laboratory of Structural Chemistry, Fujian Institute of Research on the Structure of Matter, Chinese Academy of Sciences, Fuzhou, Fujian 350002, China

[a] Email: dailidong@vip.gyig.ac.cn

ABSTRACT

This study reported a pressure-induced metallization for molybdenum tellurium under different pressure environments up to ~25.9 GPa through a series of experiments and first-principles theoretical calculations. This metallization was closely related to the gradual closure of bandgap rather than the structural phase transition. Under the non-hydrostatic environment, the metallization point was ~12.5 GPa and irreversible, while it occurred at a higher pressure of ~14.9 GPa and was reversible under the hydrostatic environment. We ascribed these discrepancies to the strong deviatoric stress, which reinforced the Te-Te interactions and caused the permanent plastic deformation of the interlayer spacing.

I. INTRODUCTION

Due to some promising and widespread industrial applications, AB₂-type (A=Mo, W; B=S, Se, Te) transition-metal dichalcogenides (TMDs) have attracted considerable interest in their optical, structural and electrical transport properties. At ambient conditions, most of these binary dichalcogenides belong to semiconductor with the characteristic layered structure, which is usually composed of the stacking of chalcogen-metal-chalcogen sandwiched trilayers by the interlayer van der Waals (vdW) forces along the c-axis orientation.[1–3] In the case of employing high pressure on these materials, their corresponding physical properties can be greatly changed, such as structural phase transition, amorphization and metallization.[4–10] These displayed unique high-pressure behaviors for transition-metal dichalcogenides have vital significance to develop some innovative optoelectronic devices.

Molybdenum tellurium (MoTe₂) is a typical layered semiconductor material with an indirect bandgap energy of ~1.0 eV. Like most of TMDs, it was also found to undergo the pressure-induced metallization, but there exist some controversial viewpoints on its metallization pressure point in the previously reported results. Rifliková et al. performed the first-principles theoretical calculations on MoTe₂ up to 30.0 GPa to investigate its electrical transport properties, and revealed a pressure-induced metallization at above 13.0 GPa.[5] By contrast, Bera et al. think that the metallization of MoTe₂ occurred at ~6.0 GPa according to their high-pressure Raman spectroscopy results up to 29.0 GPa.[11] In addition, the pressure environment has been reported to be another critical factor in affecting the structural phase transition, the metallization pressure point and as well as the reversibility of metallization for the layered TMDs (e.g. WS₂, MoS₂ and MoSe₂).[10,12,13] However, as for

MoTe$_2$ with the highly similar layered structure, there is still lack of relative investigation on the effect of the pressure environment on its high-pressure properties till now. In this present studies, we revealed that MoTe$_2$ exhibited diverse metallization phenomenon under non-hydrostatic and hydrostatic environments. Furthermore, a reasonable explanation for these observed discrepancies under different pressure environments was provided, and the metallization mechanism was also detailedly clarified.

II. EXPERIMENTAL

MoTe$_2$ powders with a high purity of 99.99% were commercially purchased from Leshan Kaiyada limited company. High pressure was generated by the diamond anvil cell (DAC) with anvil culet size of 300 µm. Helium was selected as the pressure medium to obtain the hydrostatic environment, and no pressure medium was adopted for the non-hydrostatic environment. The pressure in the sample chamber was accurately calculated with a classic ruby pressure calibration equation by Mao *et al.*[14] The pressure calibration of ruby showed a very good accuracy (less than 5% for the non-hydrostatic condition and 3% for the hydrostatic condition). The electrical conductivity of sample was measured by a Solartron-1260 impedance/gain phase analyzer in the frequency range from 10^{-1} to 10^7 Hz. Raman scattering experiments were performed in a Renishaw 2000 micro-confocal Raman spectrometer with the laser power of ~20 mV. Some microscopically structural and morphological analysis for the starting and recovered samples were conducted through the high-resolution transmission electron microscopy (HRTEM; Tecnai G2 F20 S-TWIN TMP) and atomic force microscopy (AFM; Multimode 8 mass spectrometer, Bruker), respectively. The first-principles theoretical calculations were performed in the Material Studio package with the CASTEP code. The cutoff energy of and K-point grid were set to 950 eV and 17×17×5, respectively. The space group and atomic positions in the unit cell for MoTe$_2$ were described in Table S1 of the supplementary material. Details of the measurement procedures and calculation methods have been reported previously.[15–18]

III. RESULTS AND DISCUSSION

Figures 1(a)–(c) displayed the typical impedance spectra for MoTe$_2$ under the non-hydrostatic environment up to ~25.9 GPa and room temperature. It can be clearly seen that the impedance spectra exhibits two distinct semicircular arcs in the first quadrant from ~0.3 to ~8.1 GPa, while the impedance spectra appears only in the fourth quadrant from ~9.6 to ~25.9 GPa. This abrupt change may represent the pressure-induced electronic polarization for MoTe$_2$.[19] Figure 1(d) shows the pressure dependence of the electrical conductivity for MoTe$_2$ at room temperature, which can be divided into three distinct regions according to the slope variation of electrical conductivity upon compression: (i) at 0.3–6.4 GPa, the electrical conductivity for MoTe$_2$ gradually increases with a slope of ~0.180 S cm^{-1} GPa^{-1}; (ii) at 6.4–12.1 GPa, the electrical conductivity of sample exhibits a rapidly increasing tendency, and the corresponding slope is ~0.402 S cm^{-1} GPa^{-1}; (iii) at 12.1–25.9 GPa, it slowly increases to a relatively high value of ~0.10 S cm^{-1}
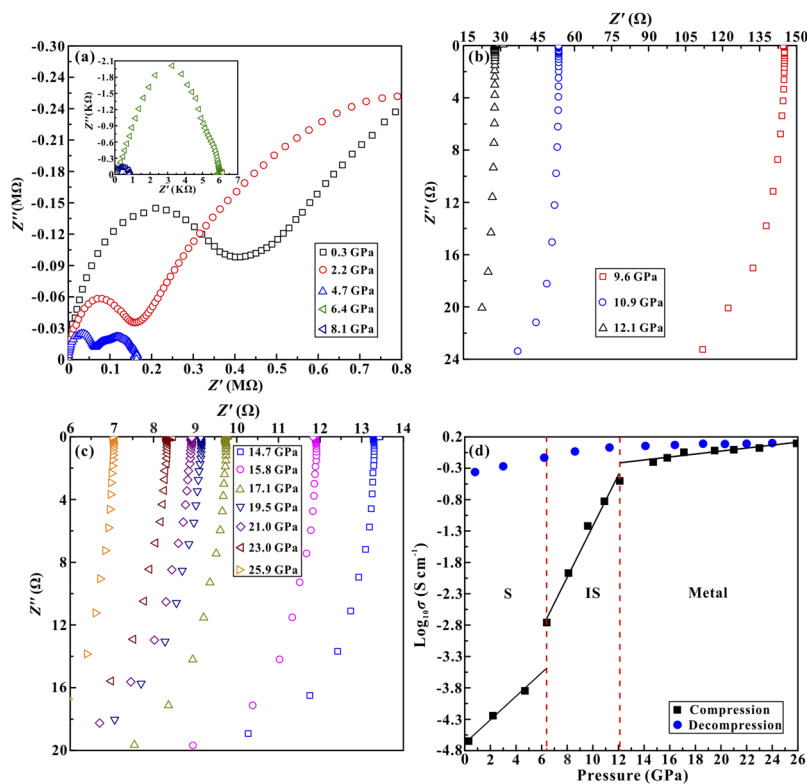
FIG. 1. (a)–(c) Typical impedance spectra of MoTe$_2$ under high pressure up to ~25.9 GPa and at room temperature. (d) The logarithm of electrical conductivity for MoTe$_2$ as a function of pressure. S: semiconductor. IS: intermediate state.

with a slope of 0.023 S cm^{-1} GPa^{-1}. At ~6.4 GPa, the abrupt increase of electrical conductivity indicates the occurrence of the intermediate state (IS) for MoTe$_2$, which is possibly correspondent to the semi-metal state with a small bandgap energy. In fact, some other AB$_2$-type transition-metal dichalcogenides have also been reported to undergo an intermediate state under high pressure.[12,20] At ~12.1 GPa, the change in the value of electrical conductivity for MoTe$_2$ is smaller than in a typical semiconductor-metal transition as reported by Errandonea *et al.*[21] However, an obvious slope change of electrical conductivity can be observed, which provides an important clue to characterize a pressure-induced metallization for MoTe$_2$ at ~12.1 GPa. Upon decompression, the electrical conductivity of MoTe$_2$ still retains a relatively high value, indicating that the metallization is irreversible under the non-hydrostatic environment.

To further check the irreversibility of metallization for MoTe$_2$ under the non-hydrostatic environment, the temperature-dependent electrical conductivity measurements were conducted at different pressure points. It is general that the electrical conductivity of semiconducting material will increase with the rise of temperature owing to the much more thermally activated charge carrier, while the opposite dependence relation for the metallization of semiconductor will appear due to the phenomenon of the increasing possibility for electron-phonon scattering effect.[22,23] As shown in Figs. 2(a)–(c), the electrical conductivity of sample shows a positive temperature dependence below ~12.5 GPa, representing typical semiconducting characteristics. However, a negative relationship between electrical conductivity and temperature is observed above ~12.5 GPa, which implies the semiconducting phase transforms to be a metallic state. The plotted contour map between the temperature, pressure, and electrical conductivity and the variation of transport activation

energy with pressure further reveal the occurrence of metallization for MoTe$_2$ at around 12.5 GPa (Fig. S1). Upon decompression, it can be seen from Fig. 2(d) that MoTe$_2$ still exhibited a metallic behavior, providing another critical evidence for the irreversible metallization of MoTe$_2$ under the non-hydrostatic environment. In addition, as for the hydrostatic environment, some crucial viewpoints and results have already been obtained as follows: (i) in comparison with the non-hydrostatic environment, the pressure point metallization of MoTe$_2$ is occurred at a relatively higher pressure of ~14.9 GPa; (ii) in opposite, the metallization of MoTe$_2$ is reversible as presented in Fig. S2.

With regard to these discrepancies displayed on MoTe$_2$ under different pressure environments, it can be reasonably explained by the deviatoric stress. For the non-hydrostatic environment, there exists a strong deviatoric stress in the sample chamber upon compression. On one hand, the strong deviatoric stress can promote the occurrence of metallization for MoTe$_2$ by accelerating the reduction of interlayer spacing. One the other hand, it can greatly strengthen the interlayer interactions among neighboring Te atom layers, which prevents the interlayer distance from recovering to its original magnitude upon decompression, and thus leads to the irreversible metallization. However, owing to the incorporation of He pressure medium into the interlayer under the hydrostatic environment, it might alleviate the interlayer coupling and the crystalline compressibility, and finally results in the hysteresis of metallization and the reversible metallization phenomenon.

The vibrational properties of MoTe$_2$ were investigated under different pressure environments up to ~25.8 GPa by Raman scattering measurements. At ambient conditions, two in-plane vibrational modes for MoTe$_2$ are observed at peak positions of 118.6 cm^{-1}
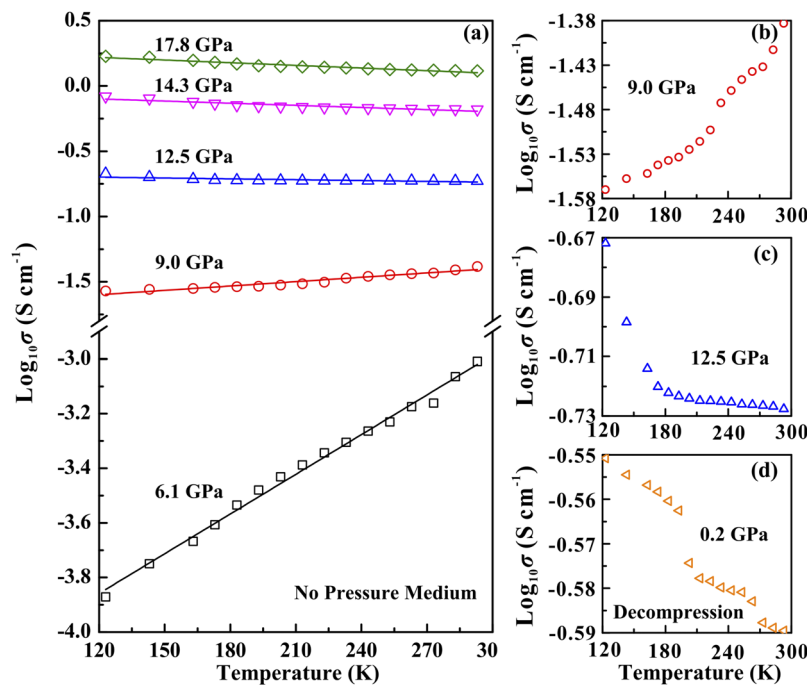

FIG. 2. (a) The temperature dependence of the logarithm of electrical conductivity for MoTe$_2$ at a series of pressure points under the non-hydrostatic environment. (b) and (c) The magnification of Log$_{10}$ σ-T curves at ~9.0 and ~12.5 GPa, respectively. (d) The metallic state of sample after decompression.

and 232.2 cm^{-1}, which correspond to the E_{1g} and $E1$ $2g$ Raman-active modes, respectively [Fig. 3(a)]. At the same time, an out-of-plane mode and another secondary order vibrational peak are also obtained at A_{1g} (171.5 cm^{-1}) and M1 (139.0 cm^{-1}), respectively. In this work, our obtained results on the Raman peak positions for MoTe$_2$ are very close to the previous data.[11,24] Under the non-hydrostatic environment, two discontinuous points can be apparently observed at pressures of ~6.2 GPa and ~12.0 GPa from the pressure dependence of Raman shifts for four vibrational modes and the corresponding fitting results [Fig. 3(b) and Table S2]. At ~6.2 GPa, Raman modes of $E1$ $2g$, A_{1g}, E_{1g} abruptly shift to higher wave numbers, and meanwhile, the M1 mode disappears. At ~12.0 GPa, all of these modes for $E1$ $2g$, A_{1g} and E_{1g} exhibit notable discontinuities, and accompanied by the appearance of a new peak (marked as M2). These results clearly indicate that MoTe$_2$ undergoes two transformations from semiconductor (S) to the intermediate state (IS) to metal at ~6.2 GPa and ~12.0 GPa, respectively. Under the hydrostatic environment, as presented in Figs. 3(c) and 3(d), and Table S3, two transition points are determined to be ~6.6 GPa and ~14.6 GPa, which are relatively higher than that under the non-hydrostatic environment. The obvious hysteresis of metallization for MoTe$_2$ under the hydrostatic environment is possibly related to the alleviated deviatoric stress by the incorporation of pressure medium into the layers, which is in consistent with our above-mentioned electrical conductivity results.

In order to deeply explore the microscopically structural and morphological variations after metallization, the starting and

recovered MoTe$_2$ samples were analyzed by HRTEM and AFM images. From the HRTEM image of the starting sample displayed in Fig. 4(a), the (002) orientational crystalline planes of MoTe$_2$ can be clearly observed with a interlayer spacing of ~0.69 nm, which is in good agreement with previously reported data.[25] In comparison with the starting MoTe$_2$, the recovered sample under the non-hydrostatic environment exhibit a relatively small interlayer spacing of ~0.31 nm, but for the hydrostatic environment, the recovered MoTe$_2$ has a similar interlayer spacing with a value of ~0.68 nm [Figs. 4(b) and 4(c)]. At the same time, to further reveal the structural changes after metallization, we also presented the fast Fourier transform (FFT) images in the inset diagram of Figs. 4(a)–(c). For the starting sample, a series of well-identified diffraction spots are observed in the FFT, indicating the high crystallinity and symmetry for the starting sample of MoTe$_2$. A similar electronic diffraction characteristic is obtained for the recovered MoTe$_2$ under the hydrostatic environment, which implies the well-preserved crystal structure upon decompression. By contrast, for the recovered sample under the non-hydrostatic environment, the diffraction spots are relatively blurry and weak, suggesting the low-degree hexagonal symmetry for MoTe$_2$. Besides, some obvious differences of the surface morphology between the starting and recovered samples are obtained from the AFM analysis in Figs. 4(d)–4(f). The surface morphology of the starting and recovered samples under the hydrostatic environment exhibit some discernible layered structures, however, as for the non-hydrostatic environment, the layered structure of the recovered sample is completely destroyed and becomes very lumpy. All of these obtained results from HRTEM and AFM on MoTe$_2$ can
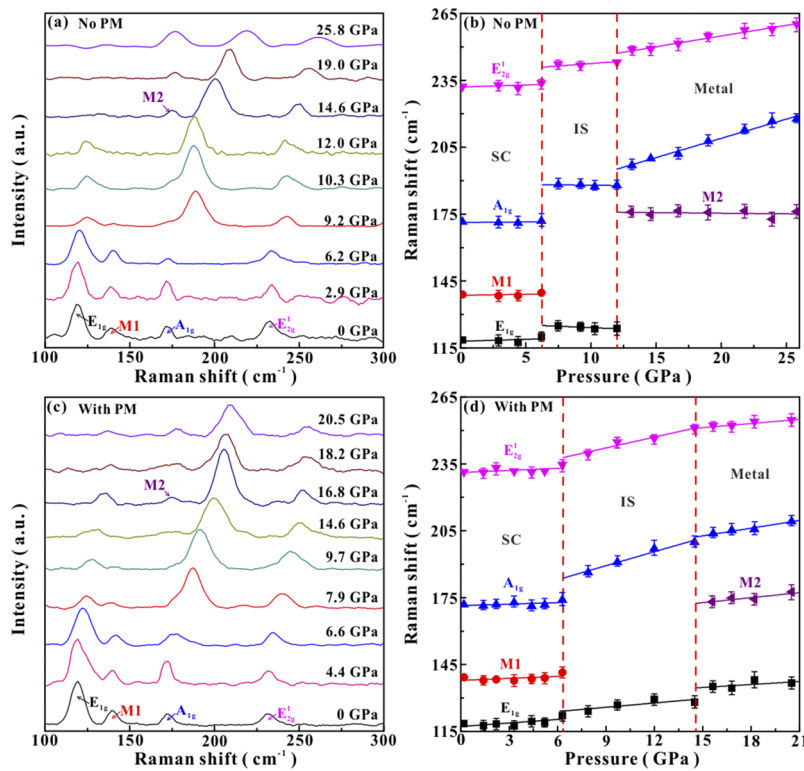
FIG. 3. (a) and (c) Raman spectra of MoTe$_2$ under high pressure up to ~25.8 GPa under non-hydrostatic and hydrostatic environments, respectively. (b) and (d) The corresponding plots of Raman shifts versus pressure. PM: pressure medium.
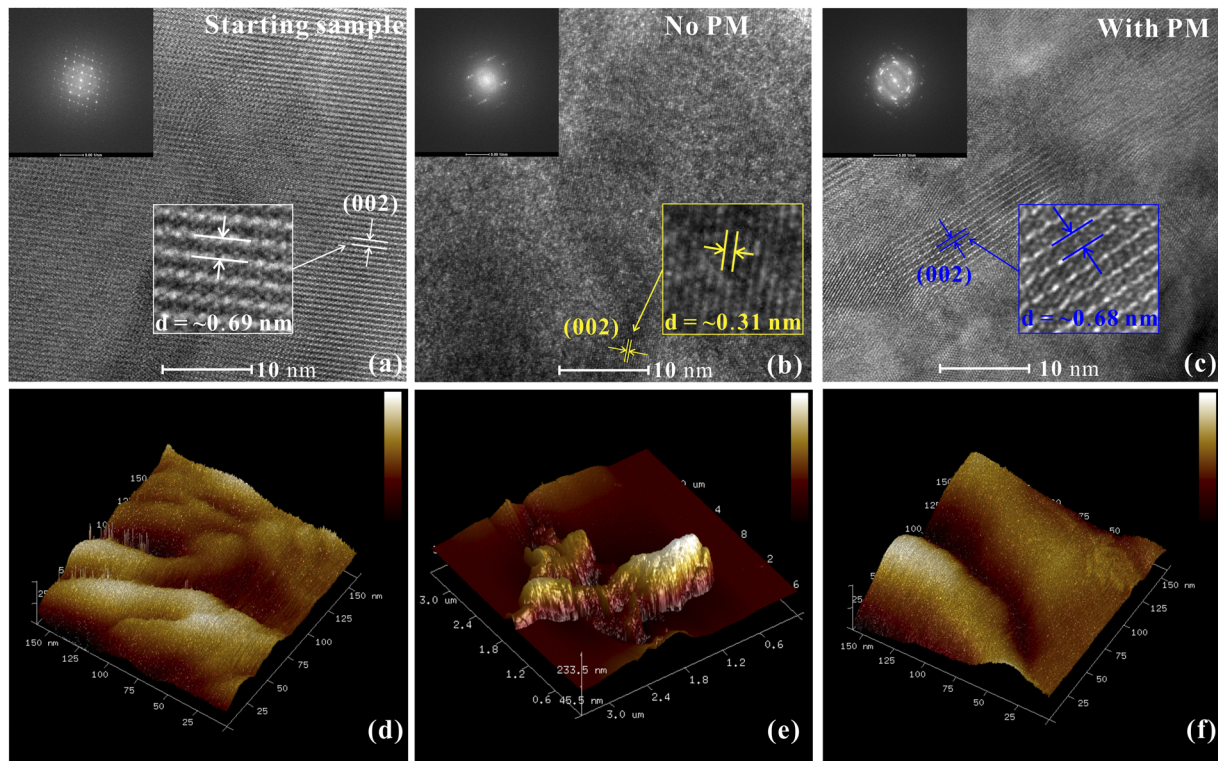
FIG. 4. (a)–(c) HRTEM images of the starting MoTe$_2$, the recovered sample under the non-hydrostatic environment from ~25.0 GPa, and the decompressed sample under the hydrostatic environment from ~22.3 GPa, respectively. The inset images in the upper left represent the fast Fourier transform (FFT) images. (d)–(f) AFM images of the initial MoTe$_2$, the decompressed MoTe$_2$ from ~24.5 GPa under the non–hydrostatic environment and ~23.8 GPa under the hydrostatic environment, respectively. PM: pressure medium.

provide some robust evidences for the reversibility of metallization under different pressure environments.

The high-pressure evolution of the crystal and electronic structure for MoTe$_2$ were explored by the first-principles theoretical calculations. As shown in Fig. 5(a), the calculated bandgap energy of MoTe$_2$ is ~0.91 eV at ambient conditions, which is slightly lower by ~0.1 eV than the previously reported data.[26,27] As usual, the bandgap energy is underestimated by the density functional theory (DFT) calculations.[28] With increasing pressure, the bandgap energy of sample gradually decreases, and then reached ~0 eV at ~13 GPa [Figs. 5(a) and 5(b)]. Meantime, the top of the valence bands (VB) that dominated by the Te-p and Mo-d electronic orbits gradually expanded towards the bottom of the conduction bands (CB) with the rise of pressure, and finally a narrow overlap between VB and CB is observed at ~13 GPa (Fig. S3). And thus, all of these calculated results clearly indicate the occurrence of metallization at ~13 GPa, which agrees well with the experimental pressure point of metallization. As plotted in Figs. 5(c) and 5(d), all of these characteristic parameters including the calculated a/a_0, c/c_0 and unit cell volume exhibit some continuous variations with pressure, and therefore, making it clear that the hexagonal phase for MoTe$_2$ still remains stable up to ~24 GPa. In conclusion, we consider that the pressure-induced metallization for MoTe$_2$ is possibly related to the

gradual closure of bandgap under high pressure rather than the structural phase transition.

Furthermore, the third order Birch Murnaghan equation of state was selected to fit our obtained results of the pressure and unit cell volume by the data of First-principle theoretical calculations, and the equation was displayed as follows,

$$P = \frac{3B_0}{2}\left[\left(\frac{V_0}{V}\right)^{\frac{7}{3}} - \left(\frac{V_0}{V}\right)^{\frac{5}{3}}\right]\left\{1 + \frac{3}{4}\left(B'_0 - 4\right)\left[\left(\frac{V_0}{V}\right)^{\frac{2}{3}} - 1\right]\right\}$$

where V_0, B_0 and B_0' represent the unit cell volume, bulk modulus and first-order derivative of the bulk modulus at zero pressure, respectively. As shown in Fig. 5(d), at the pressure range of 0–4 GPa, these values of the fitted unit cell volume and the bulk modulus for the semiconducting MoTe$_2$ at zero pressure are determined to be ~164.16 Å^3 and ~22.90 GPa, respectively. At 6–12 GPa, the corresponding unit cell volume and bulk modulus at zero pressure for the intermediate state are ~58.53 GPa and ~152.83 Å^3. At 14–24 GPa, the unit cell volume and bulk modulus at zero pressure for the metallic sample are obtained to be ~77.10 GPa and ~147.95 Å^3. In addition, we find that in comparison with the semiconducting and intermediate state, a relatively high value of bulk modulus for
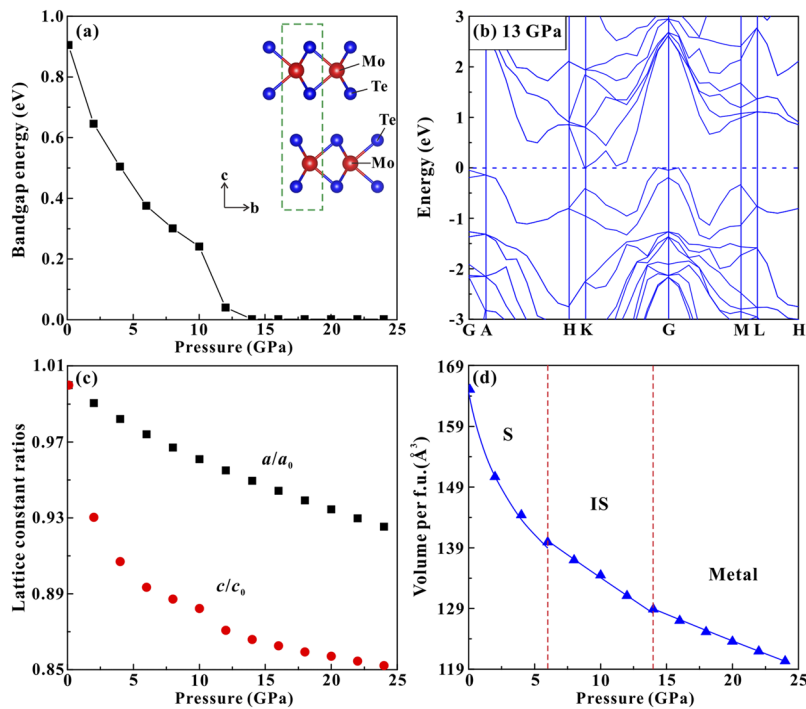
FIG. 5. (a) The pressure dependence of bandgap energy of MoTe$_2$ up to ~24 GPa from theoretical calculations. Inset: the crystal structure of the hexagonal MoTe$_2$ in the view of bc plane. (b) The bandgap structure of MoTe$_2$ at the transition point of ~13 GPa. (c) and (d) The calculated lattice parameter ratios (a/a_0 and c/c_0) and unit cell volume of MoTe$_2$ with increasing pressure, respectively.

the metallic MoTe$_2$ is realizing a low compressibility at the pressure larger than 14 GPa.

IV. CONCLUSIONS

In summary, the high-pressure evolutions of the electrical transport, vibrational and structural properties for MoTe$_2$ were systematically investigated under different pressure environments up to ~25.9 GPa. The irreversible and reversible metallization of MoTe$_2$ were confirmed under the non-hydrostatic and hydrostatic environment, respectively. For the phase transition of metallization, it was closely interrelated with the gradual closure of bandgap rather than the structural phase transition. Furthermore, as for the reversibility of metallization under different pressure environments, we attributed it to the effect of deviatoric stress, which played an important role in adjusting the Te-Te interactions and the interlayer spacing.

SUPPLEMENTARY MATERIAL

See supplementary material for the details of the contour map (between the temperature, pressure and the logarithm of electrical conductivity), the variation of activation energy with pressure, the temperature-dependent logarithm of electrical conductivity under the hydrostatic environment and the density of state for MoTe$_2$.

ACKNOWLEDGMENTS

REFERENCES

[1] A. Carvalho, R. M. Ribeiro, and A. H. Castro Neto, Phys. Rev. B **88**, 115205 (2013).

[2] A. P. Nayak, T. Pandey, D. Voiry, J. Liu, S. T. Moran, A. Sharma, C. Tan, C. H. Chen, L. J. Li, M. Chhowalla, J. F. Lin, A. K. Singh, and D. Akinwande, Nano Lett. **15**, 346 (2015).

[3] J. Gusakova, X. Wang, L. L. Shiau, A. Krivosheeva, V. Shaposhnikov, V. Borisenko, V. Gusakov, and B. K. Tay, Phys. Status Solidi A **214**, 1700218 (2017).

[4] Z. H. Chi, X. M. Zhao, H. Zhang, A. F. Goncharov, S. S. Lobanov, T. Kagayama, M. Sakata, and X. J. Chen, Phys. Rev. Lett. **113**, 036802 (2014).

[5] M. Rifliková, R. Martoňák, and E. Tosatti, Phys. Rev. B **90**, 035108 (2014).

[6] X. Wang, X. Chen, Y. Zhou, C. Park, C. An, Y. Zhou, R. Zhang, C. Gu, W. Yang, and Z. Yang, Sci. Rep. **7**, 46694 (2017).

[7] L. Hromadova, R. Martonak, and E. Tosatti, Phys. Rev. B **87**, 144105 (2013).

[8] L. Dai, Y. Zhuang, H. Li, L. Wu, H. Hu, K. Liu, L. Yang, and C. Pu, J. Mater. Chem. C **5**, 12157 (2017).

[9] M. Brotons-Gisbert, A. Segura, R. Robles, E. Canadell, P. Ordejón, and J. F. Sánchez-Royo, Phys. Rev. Mater. **2**, 054602 (2018).

[10] S. Duwal and C. S. Yoo, J. Phys. Chem. C **120**, 5101 (2016).

[11] A. Bera, A. Singh, D. V. S. Muthu, U. V. Waghmare, and A. K. Sood, J. Phys-Condens. Mat. **29**, 105403 (2017).

[12] Y. Zhuang, L. Dai, L. Wu, H. Li, H. Hu, K. Liu, L. Yang, and C. Pu, Appl. Phys. Lett. **110**, 122103 (2017).

[13] L. Yang, L. Dai, H. Li, H. Hu, K. Liu, C. Pu, M. Hong, and P. Liu, RSC Adv. **9**, 5794 (2019).

[14] H. K. Mao, J. Xu, and P. M. Bell, J. Geophys. Res. **91**, 4673, https://doi.org/10.1029/jb091ib05p04673 (1986).

[15] L. Dai, K. Liu, H. Li, L. Wu, H. Hu, Y. Zhuang, L. Yang, C. Pu, and P. Liu, Phys. Rev. B **97**, 024103 (2018).

[16] C. Pu, L. Dai, H. Li, H. Hu, K. Liu, L. Yang, and M. Hong, AIP Adv. **9**, 025004 (2019).

[17] L. Wu, L. Dai, H. Li, H. Hu, Y. Zhuang, and K. liu, J. Appl. Phys. **121**, 125901 (2017).

[18] K. Liu, L. Dai, H. Li, H. Hu, L. Wu, Y. Zhuang, C. Pu, and L. Yang, Phys. Chem. Miner. **45**, 85 (2018).

[19] Y. A. Kandrina, A. N. Babushkin, S. N. Shkerin, and Y. Y. Volkova, Defect Diffus. Forum **208-209**, 295 (2002).

[20] A. P. Nayak, S. Bhattacharyya, J. Zhu, J. Liu, X. Wu, T. Pandey, C. Jin, A. K. Singh, D. Akinwande, and J. F. Lin, Nat. Commun. **5**, 3731 (2014).

[21] D. Errandonea, A. Segura, J. F. Sánchez-Royo, and V. Muñoz, Phys. Rev. B **55**, 16217 (1997).

[22] P. G. Naumov, M. A. ElGhazali, H. Mirhosseini, V. Süß, E. Morosan, C. Felser, and S. A. Medvedev, J. Phys-Condens. Mat. **30**, 035401 (2018).

[23] R. P. Dias, M. Kim, and C. S. Yoo, Phys. Rev. B **93**, 104107 (2016).

[24] S. Sugai and T. Ueda, Phys. Rev. B **26**, 6554 (1982).

[25] A. Ouadah, J. C. Bernède, J. Pouzet, and M. Morsli, Phys. Stat. Sol. (a) **134**, 455 (1992).

[26] C. Ruppert, O. B. Aslan, and T. F. Heinz, Nano Lett. **14**, 6231 (2014).

[27] A. J. Grant, T. M. Griffiths, G. D. Pitt, and A. D. Yoffe, J. Phys. C: Solid State Phys. **8**, L17 (1975).

[28] D. Errandonea, A. Segura, F. J. Manjón, A. Chevy, E. Machado, G. Tobias, P. Ordejón, and E. Canadell, Phys. Rev. B **71**, 125206 (2005).